AIAA JOURNAL
Vol. 48, No. 1, January 2010

Numerical Simulations of Effects of Micro Vortex Generators Using Immersed-Boundary Methods

Santanu Ghosh,* Jung-Il Choi,† and Jack R. Edwards‡
North Carolina State University, Raleigh, North Carolina 27695-7910

DOI: 10.2514/1.40049

This work presents an immersed-boundary technique for compressible, turbulent flows and applies the technique to simulate the effects of micro vortex generators in controlling oblique-shock/turbulent boundary-layer interactions. The Reynolds-averaged Navier–Stokes equations, closed using the Menter k-ω turbulence model, are solved in conjunction with the immersed-boundary technique. The approach is validated by comparing solutions obtained using the immersed-boundary technique with solutions obtained on a body-fitted mesh and with experimental laser Doppler anemometry data collected at Cambridge University for Mach 2.5 flow over single micro vortex generators. Simulations of an impinging oblique-shock boundary-layer interaction at Mach 2.5 with and without micro vortex-generator flow control are also performed, considering the development of the flow in the entire wind tunnel. Comparisons are made with experimental laser Doppler anemometry data and surface-pressure measurements from Cambridge University and an analysis of the flow structure is performed. The results show that three dimensional effects initiated by the interaction of the oblique shock with the sidewall boundary layers significantly influence the flow patterns in the actual experiment. The general features of the interactions with and without the micro vortex-generator array are predicted to good accord by the Reynolds-averaged Navier–Stokes/immersed-boundary model.

Nomenclature

d, $\tilde{d}^{+,-}$	=	distance from nearest wall/immersed surface point
$d^{+,-}$	=	normalized distance
f, g	=	scaling functions
G	=	Heaviside step function based on signed distance function
h	=	height of vortex generator
k	=	turbulent kinetic energy/power law
$\boldsymbol{n}$	=	coordinate normal to immersed surface
p	=	pressure
R	=	universal gas constant
$\mathbf{R}$	=	residual vector
r	=	recovery factor
T	=	temperature
u	=	x component of velocity
$\mathbf{u}$	=	velocity vector
u_τ	=	friction velocity
$\mathbf{V}$	=	primitive variable vector
v	=	component of velocity in y direction
w	=	component of velocity in z direction
X	=	streamwise distance from start of test section
Y	=	vertical distance from lower wall
Z	=	spanwise distance measured from centerline of domain/wind tunnel
γ	=	ratio of specific heats
ε	=	dissipation
ρ	=	density
$\tilde{\rho}$	=	normalized density
Φ	=	signed distance function
ω	=	turbulence frequency

Subscripts

B	=	at band cell
I	=	at interpolation point
i	=	ith component of vector
j	=	jth component of vector
k	=	kth component of vector
N	=	normal component
NS	=	Navier–Stokes
T	=	tangential component
w	=	at wall
1, 2	=	components of vector in a plane tangential/parallel to the immersed surface

Superscripts

l	=	subiteration level
n	=	time step
$+$	=	between band cell and interpolation point
$-$	=	between immersed surface and band cell

Presented as Paper 3728 at the 38th AIAA Fluid Dynamics conference, Seattle, WA, June 2008; received 25 July 2008; revision received 24 July 2009; accepted for publication 19 Aug. 2009.

*Ph.D. Student, Campus Box 7910, Department of Mechanical and Aerospace Engineering. Student Member AIAA.

†Research Assistant Professor, Campus Box 7910, Department of Mechanical and Aerospace Engineering. Member AIAA.

‡Professor, Campus Box 7910, Department of Mechanical and Aerospace Engineering. Associate Fellow AIAA.

I. Introduction

OBLIQUE shock boundary-layer interactions (SBLIs) occurring in mixed compression engine inlets have been a cause of concern to the aerospace industry. Shock-induced separation of the boundary layer and associated unsteady effects can cause general performance losses and can even lead to engine unstart. It is thus important to control the flow either before or during the interaction process [1]. Several previous studies have examined the effectiveness of boundary-layer control devices in altering the physics of SBLIs [2–8]. A vortex generator (VG) is a boundary-layer control device which acts by introducing streamwise vortices in the flow. These vortices can energize the boundary layer by mixing the higher-momentum external flow with low-momentum flow near the wall [9]. Conventional VGs are of the height of the boundary-layer thickness whereas a micro or subboundary-layer VG is of a height approximately 40% or less of the boundary-layer thickness. The potential of micro VGs in controlling shock/boundary-layer interactions has received renewed attention [2,3,9–12]. Anderson

et al. [2] have performed optimization studies using Reynolds-averaged Navier–Stokes (RANS) calculations that show benefits of micro VG arrays in terms of increased stagnation pressure recovery and improved boundary-layer characteristics. More recently, Lee et al. [13] and Shinn et al. [14] have modeled shock/boundary-layer interactions with micro VG control using structured/unstructured body-fitted grids with RANS and large-eddy simulation methods. Several experimental investigations of micro VG control of oblique-shock/boundary-layer interactions are underway worldwide, but the most complete set of published experimental data is that collected at Cambridge University by Dr. Holger Babinsky and coworkers [9]. These experiments use Schlieren imaging, surface oil-flow measurements, pitot-pressure surveys, and nonintrusive laser Doppler anemometry (LDA) to arrive at a detailed characterization of the effects of micro VGs on boundary-layer properties with and without shock interactions.

This paper is part of a general thrust toward developing immersed-boundary (IB) methods capable of simulating the effects of various flow-control devices used in high-speed internal flows. The potential advantages of an IB method in this scope include significant economy in the number of mesh points required to render the control device (compared with body-fitted meshes), the ease with which different types of control devices can be interchanged and their effects assessed, and the ability to model moving control devices (such as mesoflaps) without mesh adaptation. An IB method that is suitable for these applications has been recently developed for incompressible flows [15]. This approach reconstructs the velocity field near immersed surfaces using a power-law function, which enables the method to approximate the energizing effects of a turbulent boundary layer. This eliminates the need for a highly resolved mesh near the immersed body. In this paper, we extend the IB method [15] to compressible, turbulent flows and couple it with the Menter k-ω turbulence model [16,17]. The combined methodology is then assessed through simulations of several of the Cambridge University experiments. The outline of this paper is as follows. Section II describes the computational model, including details of the flow solver, the turbulence closures used, and the IB method. Section III describes the problem setup, including details of the experiments simulated, and the meshing arrangement. Results of the investigation are presented in Section IV, and some conclusions are outlined in Section V.

II. Computational Methodology

The governing compressible Navier–Stokes equations are discretized in a finite-volume framework. Inviscid fluxes are discretized using a low-diffusion flux-splitting scheme (LDFSS) [18], whereas viscous and diffusive fluxes are discretized using second-order central differences. The piecewise parabolic method [19] is used to extend the first-order LDFSS upwind scheme to fourth order in smooth regions of the flow. An implicit method is used to advance the equations in time. The matrix system resulting from the linearization of the equation system is approximately solved using a planar relaxation procedure at each subiteration. The present work also extends an existing immersed-boundary method [15] to compressible, turbulent flows and couples it with the RANS solver described earlier.

A. Reynolds-Averaged Navier–Stokes Methodology

In the present study, the RANS closure used is Menter's hybrid k-ω/k-ε model [16] in its baseline (BSL) and shear stress transport (SST) forms. Specifically, the BSL model is used for RANS cases without shock impingement, and the SST model is used for the shock-interaction cases. The SST model generally increases the extent of separation relative to the BSL model, and for this case, the adoption of the SST modification results in better agreement with experimental data.

B. Immersed-Boundary Method

In the present work, the IB method developed in Choi et al. [15] is extended to handle compressible, turbulent flows. The immersed surface is generated as a cloud of points which can be structured or unstructured. The entire flow domain is then classified into three categories of cells. Cells sufficiently removed from the immersed boundary are termed as field cells, cells very near but not inside the immersed object are band cells, and cells inside the immersed body are interior cells (see Fig. A1). To perform this classification, a distance function to the nearest surface point for all cells (within a bounding box of the IB) is computed using an approximate nearest neighbor search algorithm. Concepts from computational geometry are then used to impose an unambiguous sign to the distance function (thus deciding inside or outside for closed surfaces). A direct forcing approach is used to enforce the boundary conditions at the interior and band cells. Band-cell properties are defined by interpolation of information from surrounding field cells along lines normal to the surface. This results in the residual form of the equation system shown below which is then solved implicitly, coupled with exterior cells, by use of subiteration techniques.

$$R_i^{n+1,l} = (1 - G(\Phi^{n+1}))R_{i,NS}^{n+1,l} + G(\Phi^{n+1})\left[\frac{V_i^{n+1,l} - V_{B,i}^{n+1,l}}{\Delta t}\right] \quad (1)$$

This equation represents the blending of the Navier–Stokes residual with a source term that relaxes the primitive variable vector $V = [\rho, u, v, w, T, k, \omega]^T$ to its band-cell values. The quantity $G(\Phi)$ is a sharp Heaviside function (set to 1 for band and interior cells and zero otherwise), Φ is the signed distance function, and l is a subiteration index. To extend the method to compressible flows the following first-order accurate closures are considered for the fluid properties in the band cells, in which the subscript I indicates properties obtained at an interpolation point located along a normal line extending outward from the nearest surface point to the band cell in question, and the subscript B indicates the band-cell. Procedures for determining the location of the interpolation point and the properties there are described in Ref. [15].

$$\begin{aligned} p_B &= p(d_I) \\ u_{B,i} - u_{w,i} &= u_{T,i}(d_I)\left(\frac{d_B}{d_I}\right)^k + u_{N,i}(d_I)g(\rho, d_I, d_B) \\ u_{N,i}(d_I) &= (u_j(d_I) - u_{w,j})\mathbf{n}_j\mathbf{n}_i \\ u_{T,i}(d_I) &= (u_i(d_I) - u_{w,i}) - u_{N,i}(d_I) \end{aligned} \quad (2)$$

In Eq. (2), the velocity field within band cells is split into a component tangent to the surface and a component normal to the surface. The tangential component is assumed to vary according to a power-law function of the distance away from the surface, whereas the normal velocity is chosen to satisfy a discrete continuity condition (see Appendix A). In these expressions, the choice of k allows the model to replicate a turbulent velocity profile ($k = 1/7$ or $1/9$) or a laminar profile ($k = 1$). To obtain the temperature distribution near the surface, Walz's relation for the temperature distribution within a compressible boundary layer is used [20]:

$$\begin{aligned} \frac{T_B}{T(d_I)} &= \frac{T_w}{T(d_I)} + \left(1 - \frac{T_w}{T(d_I)} + \frac{r(\gamma-1)}{2\gamma RT(d_I)}[u_{T,i}(d_I)]^2\right)\left(\frac{d_B}{d_I}\right)^k \\ &\quad - \frac{r(\gamma-1)}{2\gamma RT(d_I)}[u_{T,i}(d_I)]^2\left(\frac{d_B}{d_I}\right)^{2k} \quad \text{(isothermal wall) or} \\ \frac{T_B}{T(d_I)} &= 1 + \frac{r(\gamma-1)}{2\gamma RT(d_I)}[u_{T,i}(d_I)]^2\left(1 - \left(\frac{d_B}{d_I}\right)^{2k}\right) \\ &\quad \text{(adiabatic wall)} \end{aligned} \quad (3)$$

In this equation r is the recovery factor and $[u_{T,i}(d_I)]^2$ is the kinetic energy associated with the tangential velocity component at the interpolation point. The density in the band cells is obtained from the perfect gas law. The turbulence variables in the band cells are defined as

$$k_B = u_\tau^2/\sqrt{C_\mu} \qquad \omega_B = u_\tau/(\sqrt{C_\mu}\kappa d_B)\text{: } d^+ > 10.934$$
$$k_B = k(d_I)\left(\frac{d_B}{d_I}\right)^2$$
$$\omega_B = 60\nu_w/(0.075 d_B^2)\text{: } d^+ < 10.934 \quad \text{or} \quad k = 1$$
$$d^+ = u_\tau d_b/\nu_w \qquad u_\tau = |u_{T,i}(d_I)|/(\ell_n(d^+)/\kappa + 5.1)$$
$$\text{(iterative solution)} \tag{4}$$

The function $g(\rho, d_I, d_B)$ in Eq. (2) is determined by enforcing a discrete form of the continuity equation at each band cell. The result, for an adiabatic wall, is given as

$$g(\rho, d_I, d_B) = \frac{1}{\tilde{\rho}} \frac{\frac{d_B}{d_I} d^- \tilde{\rho}^-}{(\frac{d_B}{d_I} d^- \tilde{\rho}^- + (1 - \frac{d_B}{d_I})\tilde{\rho}^+)}$$
$$d^- = \left(\frac{d_B}{2d_I}\right)^k, \qquad d^+ = \left(\frac{1}{2}\left(1 + \frac{d_B}{d_I}\right)\right)^k$$
$$\frac{1}{\tilde{\rho}} = 1 + \frac{r(\gamma-1)}{2\gamma RT(d_I)}[u_{T,i}(d_I)]^2\left(1 - \left(\frac{d_B}{d_I}\right)^{2k}\right)$$
$$\frac{1}{\tilde{\rho}^-} = 1 + \frac{r(\gamma-1)}{2\gamma RT(d_I)}[u_{T,i}(d_I)]^2(1 - (d^-)^2)$$
$$\frac{1}{\tilde{\rho}^+} = 1 + \frac{r(\gamma-1)}{2\gamma RT(d_I)}[u_{T,i}(d_I)]^2(1 - (d^+)^2) \tag{5}$$

Details of this derivation are presented in Appendix A. Some of the cases presented later use another variant of this procedure that replaces the pressure extrapolation (the first line in Eq. (2)) with the finite-volume solution of the continuity equation within the band cells. In the formulation of the continuity equation, the mass flux is set to zero at a cell interface if the distance-function Φ changes sign across the interface. The continuity equation in the band cells evolves according to this constraint and to the specified velocity and temperature fields described earlier. This procedure ensures exact mass conservation but can sometimes lead to pressure oscillations within the band cells.

III. Problem Setup

A. Experiment Details

Experiments involving the effects of micro VGs on shock-interaction control have been performed at Cambridge University by Dr. Holger Babinsky and his students [9]. The experiments were performed at a nominal Mach number of 2.5, a stagnation temperature of 290 K, and a Reynolds number/meter of 30×10^6 . The test section in the wind tunnel is 90 mm high and 110 mm wide.

Table 1 Spanwise location of data stations for different micro VG sizes with/without shock interaction

Experiment	Spanwise data locations, Z, mm
Mach 2.5 flow over 6 mm micro VG	0.0, 4.5, 9.0, 18.0
Mach 2.5 flow over 3 mm micro VG	0.0, 2.3, 4.5, 9.0
Mach 2.5 shock/boundary-layer interaction, no control	0.0
Mach 2.5 shock/boundary-layer interaction, 3×3 mm micro VG array	0.0, 4.5, 9.0

Data collected in these experiments includes pitot pressure surveys, wall static pressure distributions, and axial-velocity profiles obtained at various streamwise and spanwise stations using LDA. This paper focuses on three of the Cambridge experiments:

1. Mach 2.5 flow over single wedge-shaped micro VGs with $h = 3$ and $h = 6$ mm (LDA velocity data, Schlieren imaging, surface oil-flow).

2. An oblique-shock/turbulent boundary-layer interaction at Mach 2.5 induced by a 7-deg wedge placed on the upper wall of the wind tunnel (LDA velocity data, surface-pressure measurements, Schlieren imaging, surface oil-flow).

3. The same oblique-shock/turbulent boundary-layer interaction with the addition of an array of three micro VGs with $h = 3$ mm upstream of the shock-impingement point (LDA velocity data, surface-pressure measurements, Schlieren imaging, surface oil-flow).

Figure 1 shows the general arrangement of the VG arrays within the wind tunnel. For the experiments considered herein, the trailing edge of each micro VG was located 109 mm downstream of the start of the test section. The leading edge of the shock generator was also placed at the start of the test section, resulting in a lower-wall shock impingement position of 159 mm, assuming inviscid flow. Velocity profiles were collected at streamwise stations of $X = 129$, $X = 189$, and $X = 249$ mm. Additional profiles were collected at $X = 89$ mm (in the absence of the VG) to determine the inflow boundary-layer characteristics and at $X = 159$ mm for the shock-impingement cases. The nominal boundary-layer thickness at the inflow plane ($X = 89$ mm) is around 6.5 mm. At each of the streamwise stations, LDA data was recorded at three or four spanwise stations as indicated in Table 1. The dimensions and alignment of the wedge-shaped micro VGs in the experiments are based on [2,9]. The immersed-boundary rendition of a single ($h = 3$ mm) VG is shown as an inset in Fig. 1.

B. Computational Domain

Three computational domains have been used for the simulations described in this work. The first domain (Domain I), used for the single

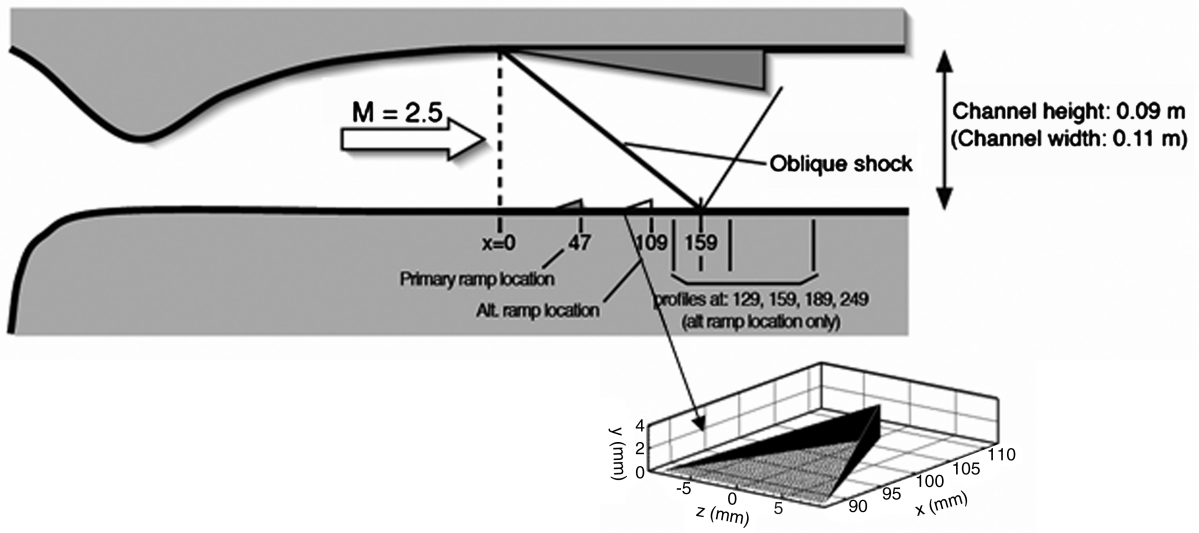

Fig. 1 Schematic of Cambridge University wind tunnel showing locations of data stations, VG positions, and shock generator (provided by H. Babinsky). Inset: IB rendition of a 3 mm VG.

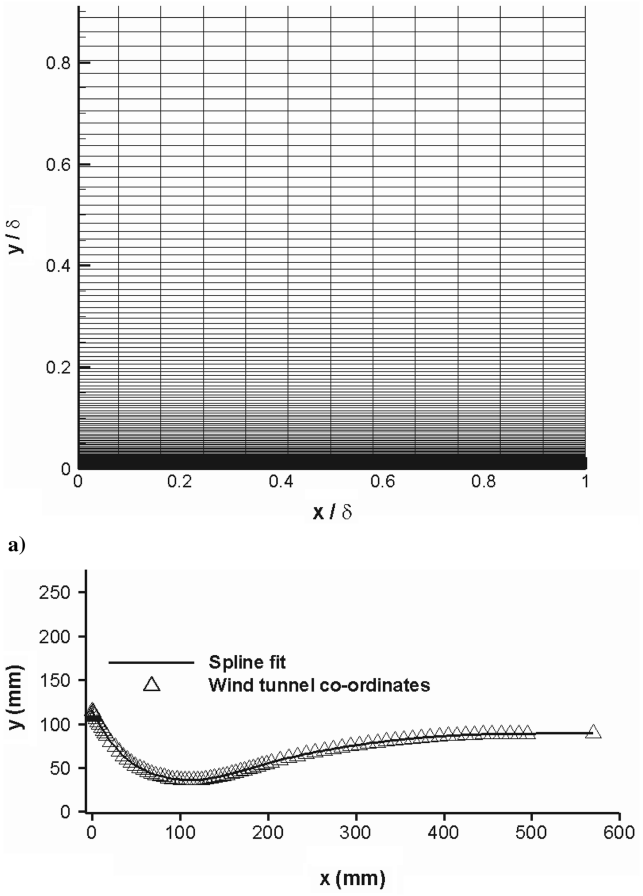

Fig. 2 a) *X-Y* view of grid (near wall) used in Domain 1, b) plot of wind-tunnel coordinates and spline fit.

micro VG calculations, ranges from $X = -108.5$mm to $X = 254.59$ mm in the streamwise direction, from $Y = 0$mm to $Y = 90$ mm in the normal direction, and from $Z = -22.5$mm to $Z = 22.5$ mm in the spanwise direction. The mesh spacing in the X and Z directions is 0.5 mm, and a minimum spacing of 0.005 mm is enforced at the lower wall. The total mesh size is $747 \times 200 \times 90 = 13.45(10^6)$ interior mesh cells. Slip wall conditions are prescribed on the upper boundary ($Y = 90$ mm), extrapolation conditions are prescribed at the outer boundary ($X = 254.59$ mm), periodic boundary conditions are applied at $Z = \pm 22.5$ mm, and no-slip, adiabatic-wall boundary conditions are applied at $Y = 0$ mm. Figure 2a shows an X-Y view of the near-wall grid with the distances normalized by the boundary-layer thickness (at the inflow plane).

To assess the effects of mesh refinement in the vicinity of an immersed-boundary rendering of a micro VG, a second domain (Domain II) having the same dimensions and boundary conditions as Domain I is also considered. The grid has same spacing as Domain I in the Y (wall-normal) direction whereas in the X and Z directions, a uniform spacing of 0.25 mm (one half of that used in Domain I) is enforced within a region surrounding the IB (from $X = 61.25$ to $X = 151.25$ mm). A patched-mesh boundary condition is used to connect this region with those up and downstream, which remain the same as in domain I. This mesh contains 23.76 (10^6) interior mesh cells.

The third computational domain (Domain III) renders the Cambridge blow-down wind tunnel in two parts. The first part encompasses one half of the entire wind tunnel, including the nozzle and test section. Coordinates of the nozzle were provided by Dr. Babinsky and were spline fitted for use in the mesh-generation exercise (see Fig. 2b). The mesh is clustered to the upper wall, the lower wall ($Y = 0$ mm), and to one side wall ($Z = 55$ mm), (centerline symmetry being assumed) with a minimum spacing of 0.005 mm. Uniform mesh spacing at a value of 0.5 mm is used from $Z = 0$ to $Z = \sim 50$ mm, and a power-law mesh-clustering function is then used to connect this spacing to the wall spacing of 0.005 mm. The mesh spacing in the X direction is 1.0 mm, and the total number of interior mesh cells is $840 \times 225 \times 130 = 24.57\,(10^6)$ cells. A steady RANS calculation was performed on this mesh to obtain accurate inflow conditions for simulations of the flow in the test section. The test-section computational domain extends from $X = -121.75$ to $X = 252.75$ mm and has a spacing of 0.5 mm in the streamwise direction. The 7-deg shock generator is placed on the upper wall in this configuration (with the leading edge at the start of the test section as in the experiment). The numbers of mesh points and the stretching patterns in the Y and Z directions are identical to that used in the full wind-tunnel grid, and the total number of interior mesh cells is $750 \times 225 \times 130 = 21.94(10^6)$ cells.

The wedge-shaped micro VGs are rendered separately as immersed boundaries using a simple structured surface mesh for each VG. The present implementation of the distance-function calculation requires a relatively fine surface mesh for accurate results. For the VG array (three 3 mm VGs) a total of 2234907 surface points is used, whereas for the 3 and 6 mm single VGs, 721785 and 2964240 points, respectively, are used.

C. Calculation Details

Convergence of the RANS calculations was ascertained using three measures: relative decrease in residual norm, constancy of surface quantities, and constancy of the global mass flow rate. All cases reached a steady-state solution. For the cases performed on Domains I and II, a flat-plate simulation at the test-section conditions was performed to determine the place at which the predicted boundary-layer properties most closely matched the experimental values at $X = 89$ mm. The inflow plane used in the calculations was then extracted from the flat-plate solution at a location 89 mm upstream of the matching position.

IV. Results

The different cases considered in this study are summarized in Table 2 and are described in detail in the subsections that follow.

A. Inflow Boundary Layer

Inflow velocity profiles were measured at $X = 89$ mm in the absence of the micro VG array. Figure 3 compares velocity profiles obtained on Domains I and III with experimental measurements. Compared with the experiment, the computed profiles show consistently larger values of velocity in the inner part of the boundary layer, which implies lower values of the displacement and momentum thicknesses. The velocity profile obtained from the wind-tunnel calculation (Domain III) is somewhat thicker than the profile obtained on Domain I.

Table 2 Summary of cases

Case	Domain	Turbulence model(s)	IB details
1. Mach 2.5 flow over 6 mm micro VG	I, II	Menter BSL	$k = 1, 1/7, 1/9$; $k = 1/7$ (mass conservative)
2. Mach 2.5 flow over 3 mm micro VG	I	Menter BSL	$k = 1/7$ (mass conservative)
3. Mach 2.5 SBLI	III	Menter SST	None
4. Mach 2.5 SBLI with micro VG array	III	Menter SST	$k = 1/7$ (mass conservative)

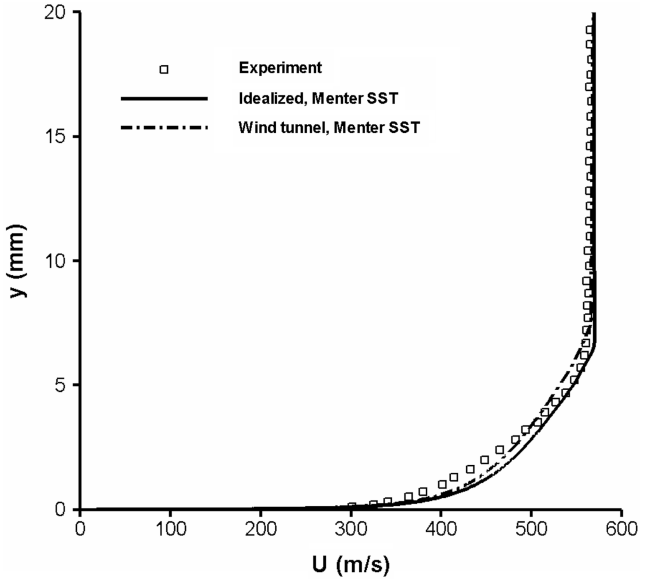

Fig. 3 Inflow velocity profiles ($X = 89$ mm).

B. Immersed-Boundary Model Assessment

To assess the immersed-boundary technique, results obtained using variations of the IB method are compared with a solution obtained on a body-fitted grid and with experimental data for Mach 2.5 flow over a 6 mm micro VG. The effect of grid refinement on the performance of the IB method is also studied by using a locally refined grid in the vicinity of the VG (Domain II). The body-fitted grid was generated using the commercial software GRIDGEN and contains 13.2 (10^6) cells, clustered to each solid surface with a minimum spacing of 0.005 mm normal to the surfaces. The X extent of the body-fitted mesh ranges from -108.5 to 224.5 mm. Contour plots of Mach number at $X = 111$ and $X = 199$ mm and centerline plots of axial velocity at $X = 129$ and $X = 189$ mm are used in the assessment. The scales for the contour plots range from 0.05 (darkest contours) to 2.85.

Mach number contours just downstream of the micro VG trailing edge at $X = 111$ mm (Fig. 4) clearly show the initial growth of the primary vortex cores. The spanwise extent of the low-momentum region is more pronounced for the $k = 1$ interpolation and is least for the solution obtained on the body-fitted mesh. The vortices lift off less in the IB solutions and spread more laterally compared with the body-fitted mesh solution. Also, the higher-momentum flow reaches closer to the wall for the body-fitted mesh solution. This implies a stronger interaction between the vortex cores and the external flow. The presence of a secondary pair of vortices formed in the near-wall region downstream of the micro VG trailing edge is indicated by darker contours near the surface. The exact shape of the wake as predicted on the body-fitted grid is not very well matched by any of the RANS IB solutions, but a trend toward improved results with lower values of k is evident. Localized X-Z mesh refinement in the vicinity of the IB seems to help in this context, with the wake behind the trailing edge of the VG being less diffused in this case compared

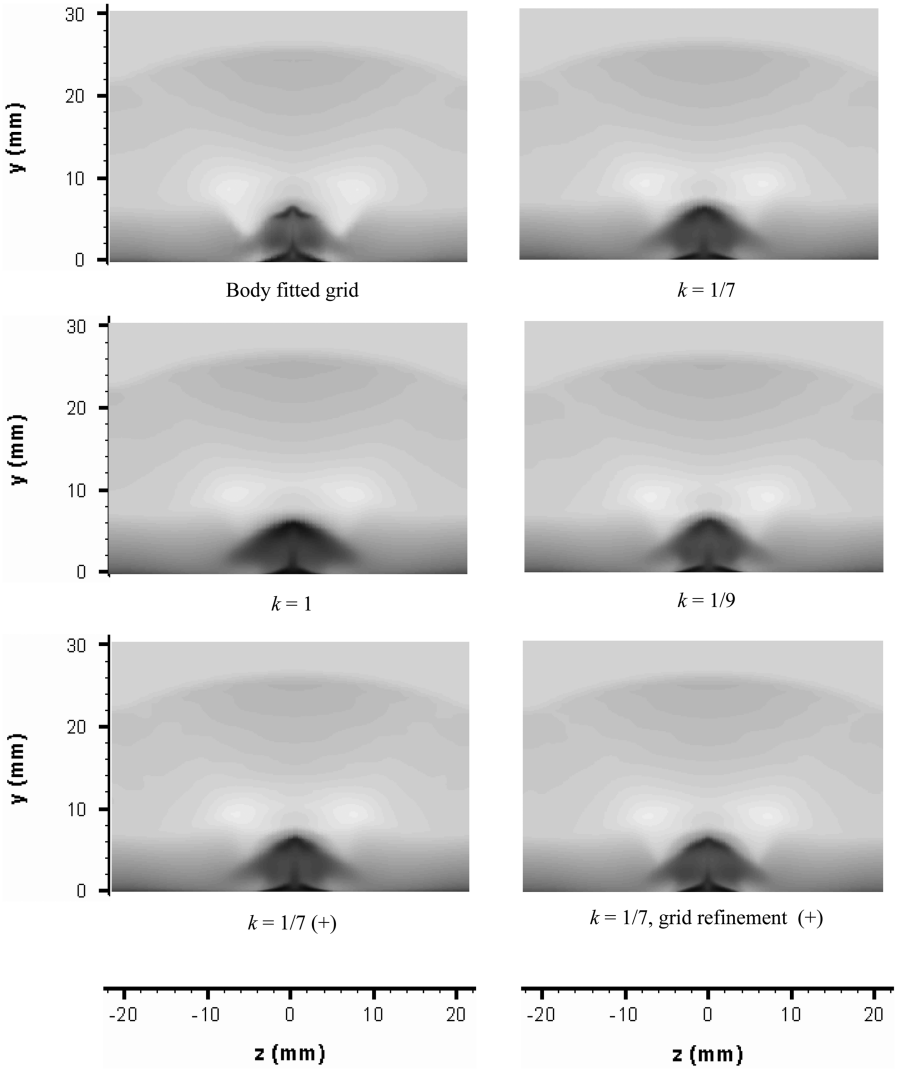

Fig. 4 Mach number contours at $X = 111$ mm for 6 mm VG placed in supersonic boundary layer (+: continuity equation integrated in band cells).

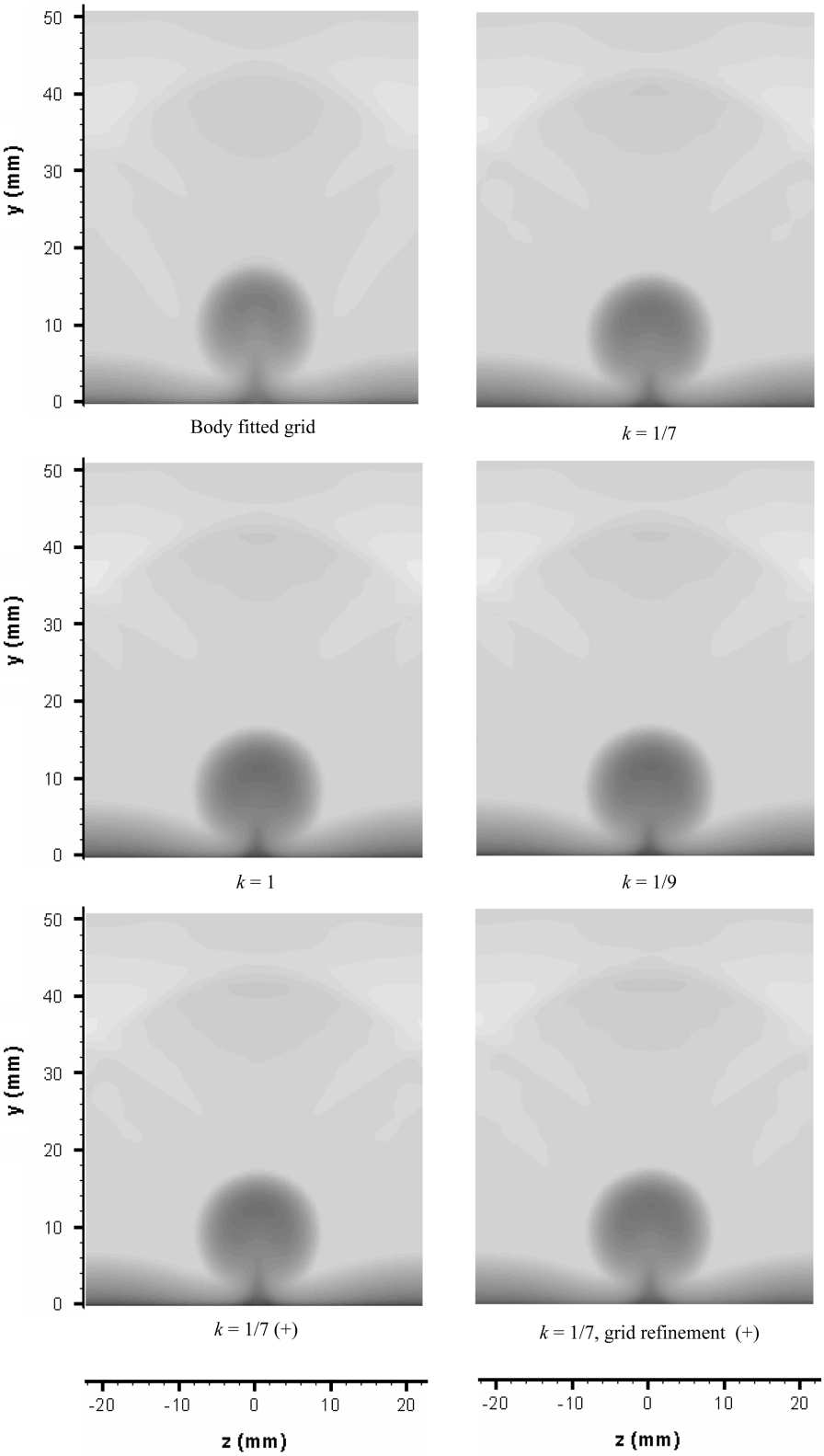

Fig. 5 Mach number contours at $X = 199$ mm for 6 mm VG in supersonic boundary layer (+: continuity equation integrated in band cells).

with the other IB solutions. Overall the mass-conservative IB predictions (using $k = 1/7$) are the closest to the body-fitted mesh RANS solutions, with the solution obtained on Domain II providing somewhat better results.

At $X = 199$ mm (Fig. 5), the vortex pairs generated behind the micro VG spread out and lift from the surface, and the lower-momentum core region becomes less pronounced, as suggested by the lighter contours. The body-fitted solution again shows a narrower and taller low-momentum region, but the differences between this solution and the IB solutions are less apparent than at $X = 111$ mm. The low-momentum region is larger for the $k = 1$ interpolation than for the others, implying that this laminar choice might not provide enough flow attachment to the micro VG surface. The solution obtained on the locally refined X-Z mesh is similar to the others in this region.

Centerline velocity profiles in Fig. 6 show that the body-fitted grid solution seems to match the experimental data best for both the stations shown. The IB predictions approach the body-fitted solution

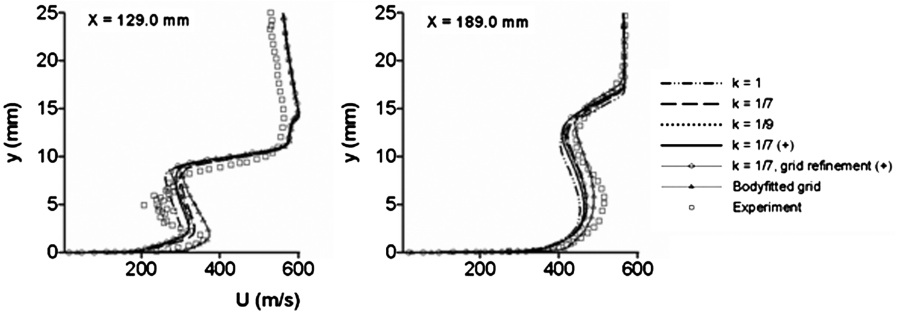

Fig. 6 Comparison of centerline axial-velocity profiles for different formulations of the IB method, a body-fitted grid, and experimental data (+: continuity equation integrated in band cells).

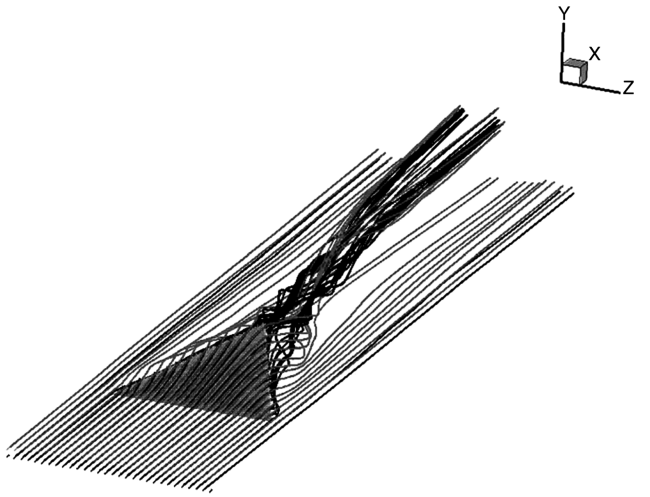

Fig. 7 Near-surface streamtraces illustrating formation of counter-rotating vortex pair (supersonic flow over a 6 mm micro VG).

for lower values of k, and interestingly, the mass-conservative IB method is not quite as accurate as the others. From the comparisons at the $X = 129$ mm station, it appears that the effects of the primary vortex in energizing the near-wall boundary layer are somewhat underpredicted by all of the IB methods. The shape of the wake deficit is not predicted well by any of the RANS methods at $X = 129$ mm but improves somewhat at $X = 189$ mm. The refined-mesh IB solution shows marginally better results for both stations in that the profiles seemed to have shifted somewhat toward the body fitted grid solutions. These results indicate that the IB rendering of the micro VG provides more of a momentum sink than does the body-fitted rendering. Considering that no effort is made to resolve the flow near the surfaces of the micro VG when the IB techniques are used, the level of agreement shown is still encouraging enough for further evaluation.

C. Detailed Data Comparisons for Mach 2.5 Flow over 6 mm and 3 mm Micro Vortex Generators

Near-surface streamtraces shown in Fig. 7 illustrate the formation of the dominant pair of counter-rotating vortices from the top surfaces of the 6 mm micro VG. Fluid very near the surface (black traces) either bypasses the micro VG entirely or is entrained into the cores of the vortices. Fluid further away from the surface either moves over the micro VG and then is forced toward the surface through the action of the vortices or is directly entrained into the vortices. Not illustrated is the formation of a secondary vortex pair very near the surface. This structure originates from a recirculation region formed just downstream of the micro VG trailing edge.

Figure 8 compares velocity profiles obtained using the RANS model ($k = 1/7$, mass-conservative IB) with LDA data collected at several X and Z positions behind the 6 mm micro VG. (see Table 1). The energizing effects of the primary vortices are reasonably well captured by the RANS model. This is reflected by the fuller velocity profiles near the wall and close to the VG ($Z = 0$ and $Z = 4.5$ mm). There is a considerable disagreement in the level of the wake deficit found at the $Z = 4.5$ mm station at $X = 129$ and $X = 189$ mm. In the experiment, the wake deficit is almost absent at this Z station, either implying less lateral spreading of the vortices or a device misalignment that shifts the time-mean position of the vortex pair. It should be noted that all measurements were taken on one side of the centerline. In an attempt to determine whether uncertainties in the placement of the laser might play a role, the RANS velocity profiles were also averaged in the Z direction over the experimental positional uncertainty of 2.5 mm.[§] These profiles show a marginal improvement with respect to the experimental data for the centerline profiles. The better agreement shown at the most downstream station ($X=$ 249 mm) for the RANS model lends support to the possibility of a slight misalignment of the micro VG with respect to the incoming flow. The level of agreement found at the more outboard stations ($Z = 9$ and $Z = 18$ mm) is generally good, though near-wall discrepancies similar to those observed for the inflow velocity profile persist.

Figure 9 presents a similar set of comparisons for Mach 2.5 flow over a 3 mm micro VG. Centerline velocity profiles from the computation do not agree particularly well with the data, in that the latter shows a much smaller wake deficit. The spanwise extent of the vortex pair is predicted to be larger than indicated in the experiment, as the measured wake deficit seems not to exist at any station other than the centerline. Agreement with experimental data further away from the vortex pair is satisfactory.

D. Wind-Tunnel Shock/Boundary-Layer Interaction

1. *Flow Structure*

A simulated Schlieren image for the impinging shock/boundary-layer interaction without micro VG control (computed at the centerplane using the vertical density gradient) is compared with an experimental image in Fig. 10. The wave patterns corresponding to the incident wave and the separation shock are comparable, but the reattachment shock angle is different. This discrepancy may be the result of line-of-sight effects, as the extent of the separation region, and thus the position of the reattachment shock, varies substantially in the spanwise direction. Figures 11 and 12 present near-surface axial-velocity contours and streamtraces. The vertical white lines in the velocity contour plots indicate the theoretical position of the shock impingement ($X = 159$ mm). The interaction of the oblique shock with the sidewall boundary layer results in a crossflow separation similar to that observed in sharp fin interactions. The downward motion of the crossflow is arrested by the flat plate, leading to the formation of vortical structures located in the sidewall/flat-plate junctures (indicated in dark contours near the upper and lower walls). The displacement effects of these structures induce the formation of a pair of separation shocks and a general movement of the flat-plate boundary-layer fluid toward the centerline. Part of the near-wall fluid lifts away from the surface at two foci of separation, located at the points of intersection of the separation shocks with the impinging oblique shock as shown in Fig. 12. This fluid then spirals through the main separation region before exiting near the centerline. The growth of the separation region toward the sidewall is prevented

[§]H. Babinsky, personal communication

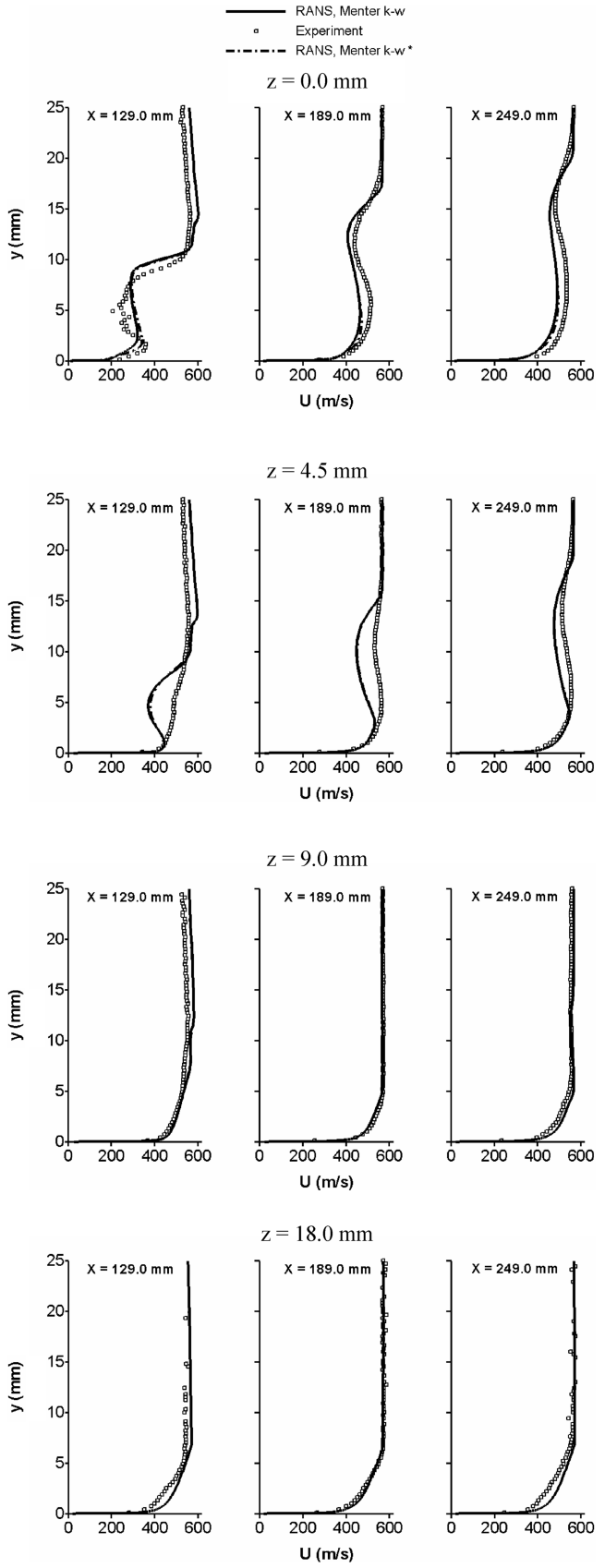

Fig. 8 Comparison of axial-velocity profiles for flow over 6 mm VG in idealized domain (∗ = data averaged over a span wise filter of 2.5 mm, centered at the *Z* location).

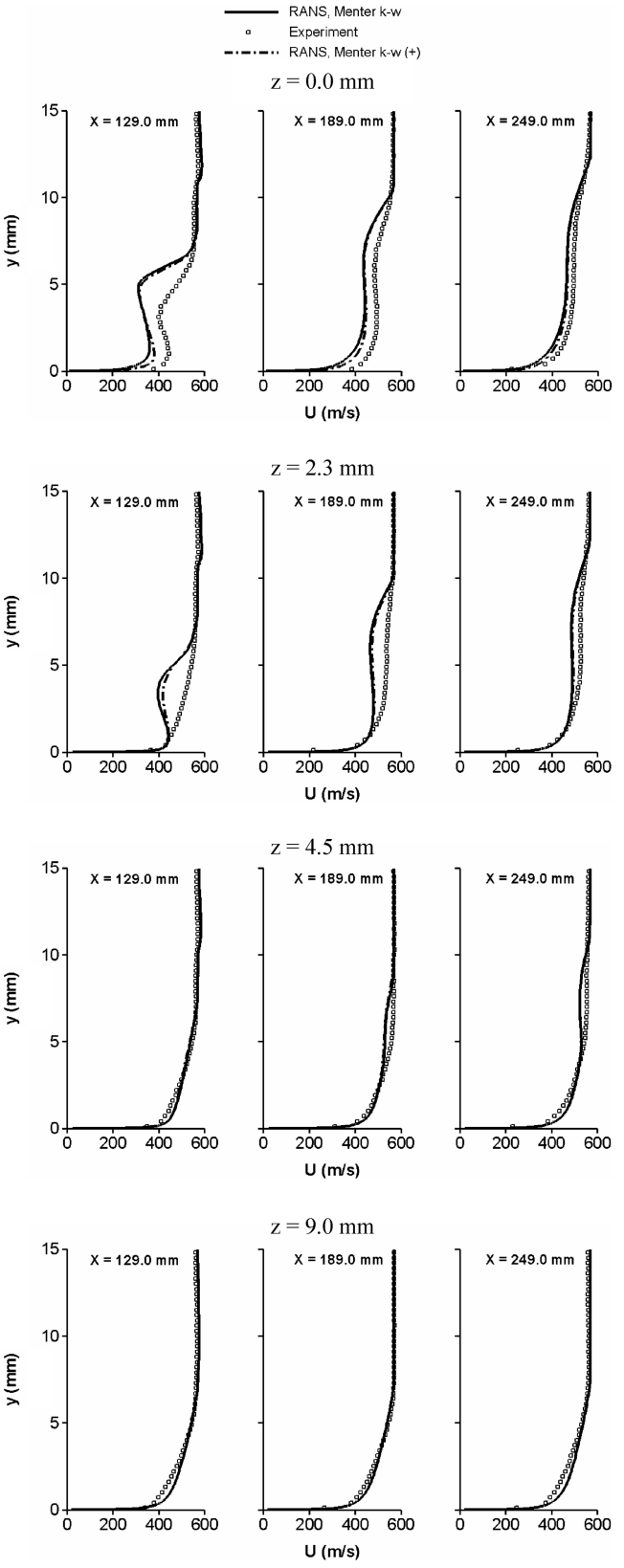

Fig. 9 Comparison of axial-velocity profiles for flow over 3 mm VG in idealized domain (∗ = data averaged over a span wise filter of 2.5 mm, centered at the *Z* location).

by the crossflow induced by the corner vortices, leading to a nonuniform region of low-momentum fluid that expands more near the centerline as shown in Fig. 11). The region of actual flow reversal is delineated by contours of zero axial velocity (shown in white lines).

2. *Comparisons with Experimental Data*

Figure 13 compares centerline surface-pressure distributions for the SBLIs with and without micro VG control with experimental data. The separation shock strength and the level of upstream influence of the interaction are predicted well by the Menter SST model for the case without the micro VG array. The predicted

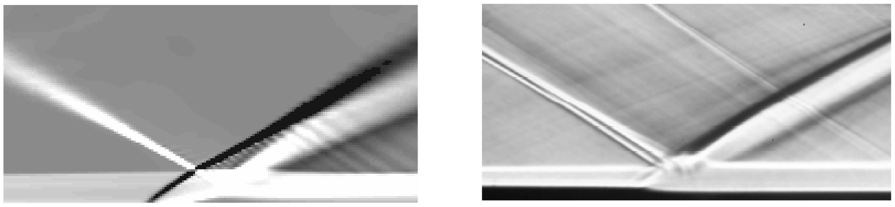

Fig. 10 Schlieren images of SBLI in wind tunnel using RANS model (left), and experiment (right).

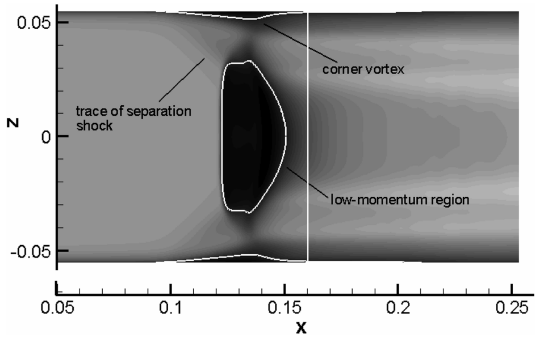

Fig. 11 Near-surface velocity contours at $Y = 0.0025$ mm (range: -5 m/s (dark) to 35 m/s) for SBLI in wind tunnel (contours reflected about centerline for clarity).

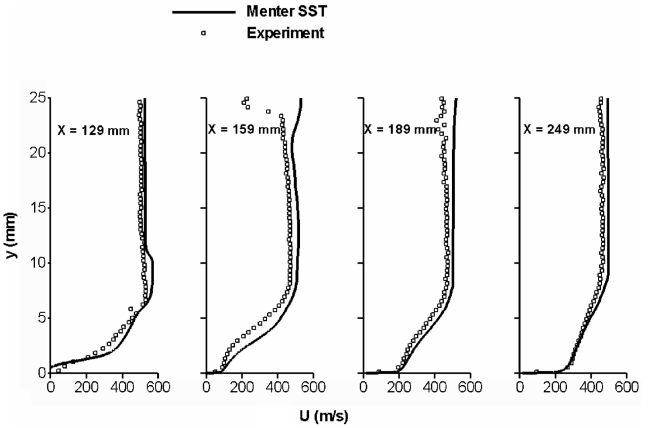

Fig. 14 Centerline axial-velocity profiles for SBLI in wind tunnel.

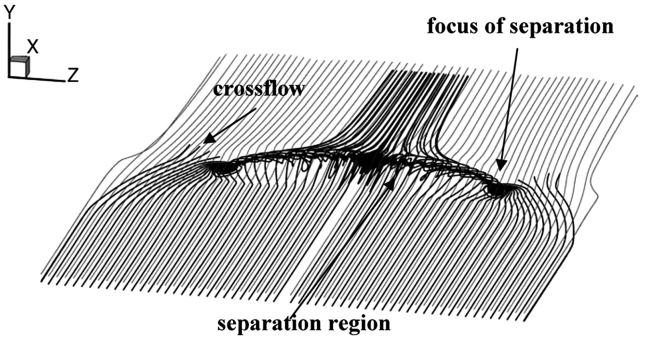

Fig. 12 Near-surface streamtraces for SBLI in wind tunnel.

pressure distribution shows the start of a plateau behind the initial pressure rise. This feature is commonly observed in stronger SBLIs but is not seen in the experimental distribution. Velocity profiles at different streamwise stations along the centerline are shown in Fig. 14. The first station ($X = 129$ mm) is within the region of upstream influence, and the predicted velocity profile contains a small region of reversed flow that is not shown in the LDA data. The comparison at $X = 159$ mm indicates that the calculation does not quite capture the shape of the wakelike velocity profile near the reattachment position. The recovery of the centerline velocity ($X = 189$ and $X = 249$ mm) is predicted very well, except for some deviations in the freestream velocity similar to those noted earlier.

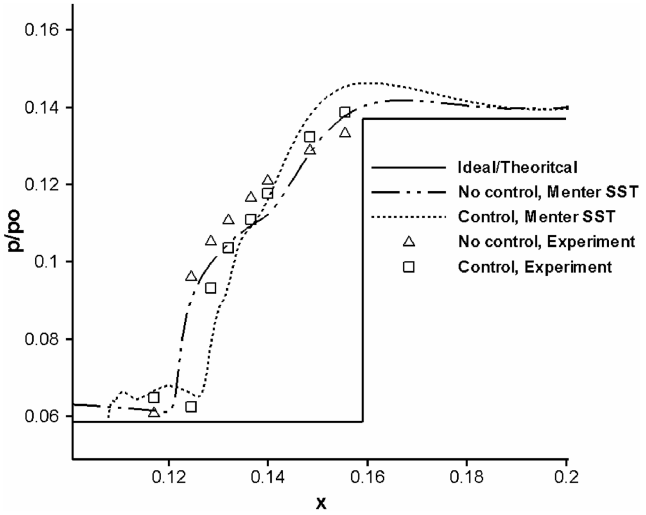

Fig. 13 Centerline surface-pressure distributions for SBLI in wind-tunnel (with/ without micro VG array).

E. Wind-Tunnel Shock/Boundary-Layer Interaction with Micro Vortex Generator Flow Control

1. Flow Structure

The effects of the micro VG array on the near-surface flow structure are illustrated in Fig. 15 (near-surface velocity contours at $Y = 0.0025$ m) and in Fig. 16 (near-wall streamtraces). Darker regions in Fig. 15 represent slower-moving fluid, whereas lighter regions represent faster-moving fluid. The major effect of the micro VG array is to induce the formation of longitudinal vortical structures (one pair per micro VG). These structures force higher-momentum fluid toward the surface, energizing the inner part of the boundary layer. The traces of the vortical structures are indicated as light bands in Fig. 15. The region directly behind the trailing edge of each micro VG is influenced by another pair of counter-rotating vortices that act to move fluid away from the surface, resulting in low-momentum streaks that also persist downstream of the interaction region.

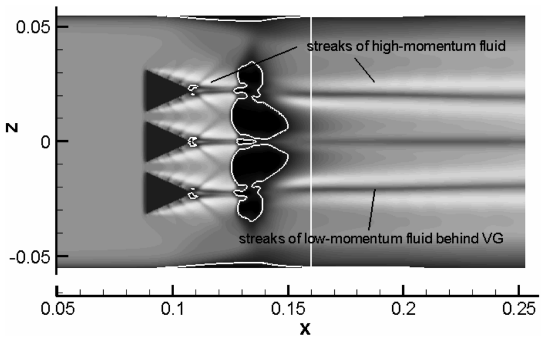

Fig. 15 Near-surface velocity contours at $Y = 0.0025$ mm (range: -5 m/s (dark) to 35 m/s) for SBLI with micro VG array in wind tunnel (contours reflected about the centerline for clarity).

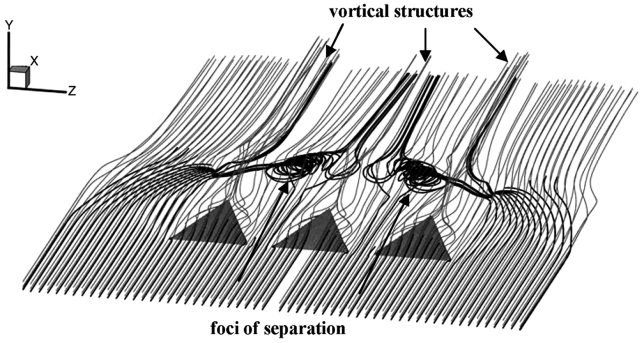

Fig. 16 Near-surface streamtraces for SBLI with micro VG array in wind tunnel.

Comparing Figs. 11 and 15, it is clear that the vortices induced by the micro VG array deform the large separation region but do not significantly reduce its size. The level of upstream influence is reduced in regions in which the counter-rotating vortices energize the near-wall boundary layer but increases in the regions between the micro VGs. The strengths of the vortices generated by the centerline micro VG appear to be reduced relative to the others, as a consequence of their interaction with the large separation region.

The black streamtraces in Fig. 16 show that part of the near-wall fluid originating between the outer VGs and the corresponding sidewalls is entrained into the vortex pairs generated from these devices. Another portion moves toward the centerline and lifts from the surface at two foci of separation, where it is entrained into the vortices generated by the centerline micro VG. Some of the near-wall fluid originating between the micro VGs is also entrained into the low-momentum region and departs from the surface at these foci. Fluid originating further away from the surface (lighter streamtraces) moves over and around the micro VGs but does not enter the low-momentum region. Some of this fluid eventually migrates into the vortical structures.

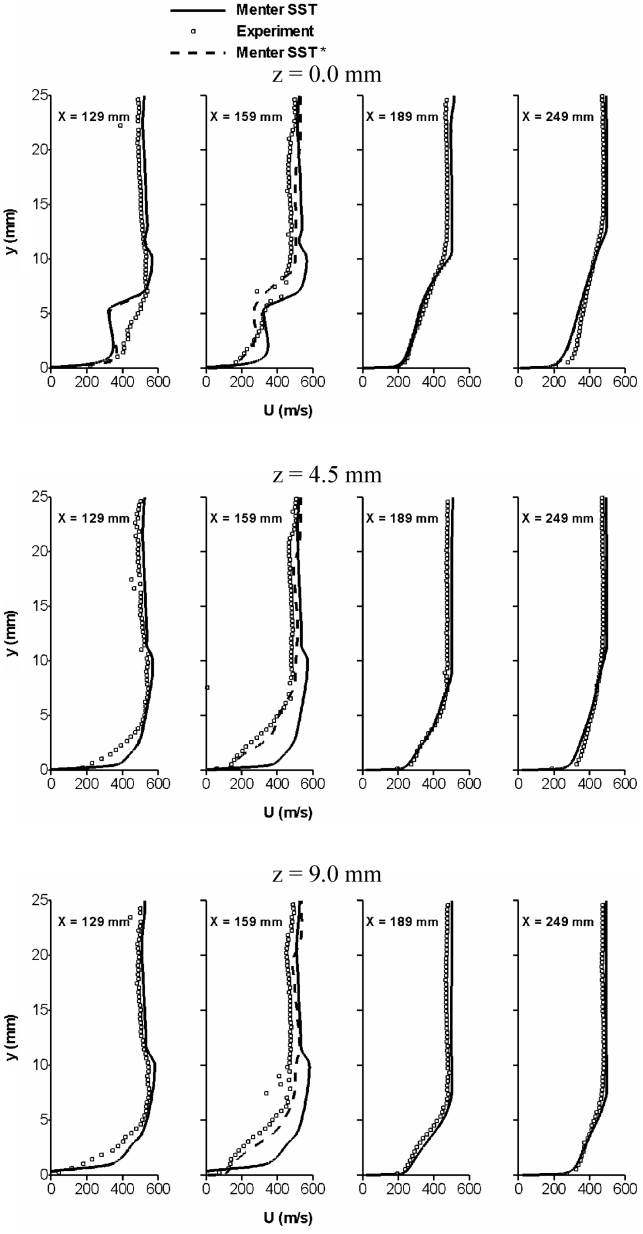

Fig. 17 Axial-velocity profiles for SBLI with micro VG array in wind tunnel (∗ indicates data averaged over a spanwise filter of 2.5 mm, centered at the *Z* location).

2. Comparisons with Experimental Data

Pressure distributions shown in Fig. 13 indicate that the effect of the micro VG array, at least at the centerline, is to reduce slightly the upstream extent of the separation region and to sharpen the pressure rise. An overshoot in pressure is observed near the reattachment location for both the calculated and measured distributions but is more pronounced in the former.

Axial-velocity predictions at several streamwise and spanwise stations are shown in Fig. 17. At the $X = 129$ and $X = 159$ mm stations along the centerline ($Z = 0$), the calculated velocity profiles show a pronounced low-momentum region that is associated with the vortex pairs. This feature is not prominent in the experimental profiles, similar to the single micro VG results. The centerline profiles further downstream are in better agreement with the experimental data. The $Z = 4.5$, $X = 159$ mm position is near the location at which the centerline vortex divides the main separation region into a smaller one located near the centerline and a larger one located further away. The topology of the flow in this region changes abruptly, and improved predictions are obtained by averaging the computed velocity profiles over the experimental laser-sheet positional uncertainty of 2.5 mm. The same is true for the data station at $Z = 9.0$, $X = 159$ mm. Agreement with the experimental data at $X = 189$ and $X = 249$ mm can be considered as excellent.

V. Conclusions

An immersed-boundary methodology valid for compressible high-speed turbulent flows is developed in this work and is combined with RANS turbulence closures (Menter's k-ω BSL and SST models). The method is used to simulate experiments performed at Cambridge University involving the control of oblique-shock/turbulent boundary-layer interactions using micro VGs. The following observations may be stated.

1) A comparison of IB predictions with those obtained on a body-fitted mesh for Mach 2.5 flow over a single 6 mm micro VG indicates that the IB techniques tend to over-predict the momentum sink effect of the VG. Results improve with the use of fractional powers ($k = 1/7$ or $1/9$) in reconstructing the velocity field near the IB. Fair agreement with experimental LDA velocity data is generally achieved for the IB method, particularly at measurement stations further away from the VG.

2) Simulations of an oblique-shock/turbulent boundary-layer interaction in the Cambridge University wind tunnel indicate that blockage effects caused by corner vortices play a significant role in the topology of the interaction. The corner vortices force boundary-layer fluid toward the centerline, leading to an elongation of the recirculation region at the centerline and a shortening of the region in the spanwise direction. Surface pressure and axial-velocity predictions using the Menter SST model are in good agreement with experimental data, but the entire wind-tunnel flow path must be simulated for accurate results.

3) The effect of a 3 mm micro VG array on the wind-tunnel shock/boundary-layer interaction is to deform the region of flow separation but not to eliminate it entirely. The vortices generated by

the micro VG array force higher-momentum fluid toward the surface, making the boundary layer more resistant to the adverse pressure gradient in regions directly contacted by the vortices. The vortices also persist far downstream of the interaction. Good predictions of axial velocity throughout the interaction region are obtained if computed velocity profiles are averaged over the experimental laser-sheet position uncertainty of 2.5 mm.

Considering that the IB method does not use high-mesh resolution close to immersed surfaces, the level of agreement with experimental data shown is encouraging. The potential of the IB technique in conducting rapid trade-off studies, in simulating moving control devices, and in reducing overall resource requirements is clear, and these aspects will be studied in future work.

Appendix: Determination of Normal Velocity Component in Band Cells

In the immersed-boundary method of Choi et al. [15], we adopt a locally parallel-flow assumption so that all flow properties in the region near the immersed surface are functions of the coordinate normal to the surface n. Decomposing the velocity into tangential components $\mathbf{u}_{T_1}$ and u_{T_2} (in directions T_1 and T_2) and normal component $\mathbf{u}_n$ (in direction n), we write the steady continuity equation as

$$\nabla_T \cdot (\rho \mathbf{u}_T) + \frac{\partial(\rho u_N)}{\partial n} = 0$$

$$\text{with } \nabla_T \cdot (\rho \mathbf{u}_T) = \frac{\partial(\rho u_{T_1})}{\partial T_1} + \frac{\partial(\rho u_{T_2})}{\partial T_2} \tag{A1}$$

Applying the parallel-flow assumption and introducing the functional forms $f(n)$ and $g(n)$ to describe the distributions in tangential velocity and density from the interpolation-point location d_I to the wall [i.e., $\mathbf{u}_T(n) = \mathbf{u}_T(d_I) f(n)$, $\rho(n) = \rho(d_I) g(n)$], we have

$$\nabla_T \cdot [\rho(d_I)\mathbf{u}_T(d_I)] f(n) g(n) + \frac{\partial(\rho u_N)}{\partial n} = 0 \tag{A2}$$

Now consider the two control volumes Ω_1 and Ω_2 shown in Fig. A2. Discretizing Eq. (A2) over each of the control volumes gives the following system:

$$\nabla_T \cdot [\rho(d_I)\mathbf{u}_T(d)] f(\tilde{d}^+) g(\tilde{d}^+) + \frac{\rho(d_I)u_N(d_I) - \rho(d_B)u_N(d_B)}{d_I - d_B} = 0$$

$$\Omega = \Omega_1$$

$$\nabla_T \cdot [\rho(d_I)\mathbf{u}_T(d_I)] f(\tilde{d}^-) g(\tilde{d}^-) + \frac{\rho(d_b)u_N(d_B)}{d_B} = 0$$

$$\Omega = \Omega_2 \tag{A3}$$

with

$$\tilde{d}^+ = (1/2)(d_I + d_B), \qquad \tilde{d}^- = (1/2)d_B \tag{A4}$$

Upon eliminating the common factor $\nabla_T \cdot [\rho(d_I)\mathbf{u}_T(d_I)]$, system (A3) can be solved to obtain an expression for the normal velocity component at the band cell, $u_N(d_B)$:

$$\frac{u_N(d_B)}{u_N(d_I)} = \frac{\rho(d_I)}{\rho(d_B)} \left(\frac{\frac{d_B}{d_I} f(\tilde{d}^-) g(\tilde{d}^-)}{\frac{d_B}{d_I} f(\tilde{d}^-) g(\tilde{d}^-) + f(\tilde{d}^+) g(\tilde{d}^+)(1 - \frac{d_B}{d_I})} \right) \tag{A5}$$

The closure is completed by substituting power law and Walz/Crocco-type relations for $f(n)$ and $g(n)$:

$$f(n) = \left(\frac{n}{d_I}\right)^k, \qquad g(n) = \frac{T_I}{T(n)} \tag{A6}$$

from Eq. (3) yielding the form shown in Eq. (5).

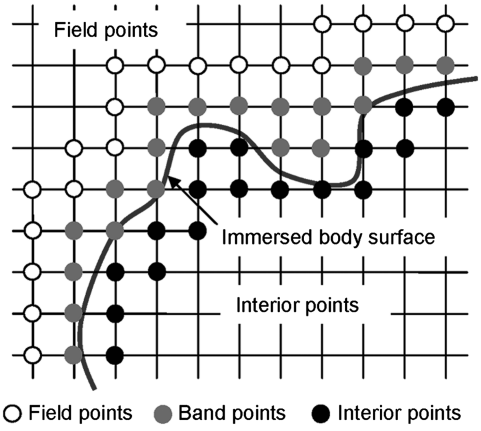

Fig. A1 Cell classification scheme for immersed-boundary method.

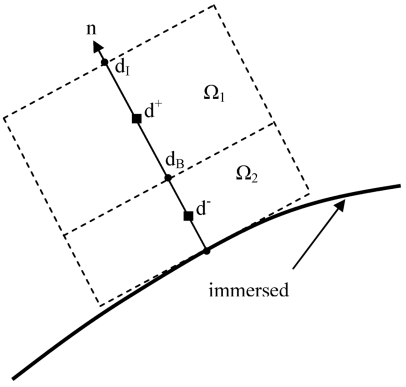

Fig. A2 Schematic of control volumes used to define normal velocity component at band cells.

Acknowledgments

This work is supported by the U.S. Air Force Office of Scientific Research under grant FA9550-07-1-0191, monitored by John Schmisseur. Computer resources have been provided by the high-performance computing component of North Carolina State University's Office of Information Technology. The authors gratefully acknowledge Holger Babinsky of Cambridge University for providing information relating to his experiments and for many helpful discussions.

References

[1] Délery, J. M., "Shock Wave/Turbulent Boundary Layer Interaction and Its Control," *Progress in Aerospace Sciences*, Vol. 22, No. 4, 1985, pp. 209–280. doi:10.1016/0376-0421(85)90001-6

[2] Anderson, B. H., Tinapple, J., and Surber, L., "Optimal Control of Shock Wave Turbulent Boundary Layer Interactions Using Micro-Array Actuation," AIAA Paper 2006-3197, June 2006.

[3] Holden, H. A., and Babinsky, H., "Vortex Generators Near Shock/Boundary Layer Interactions," AIAA Paper 2004-1242, Jan. 2004.

[4] Ashill, P. R., Fulker, J. L., and Hackett, K. C., "Research at DERA on Sub Boundary Layer Vortex Generators (SBVGs)," AIAA Paper 2001-0887, Jan. 2001.

[5] Smith, A. N., Holden, H. A., Babinsky, H., Fulker, J. L., and Ashill, P. R., "Control of Normal Shock Wave/Turbulent Boundary Layer Interactions Using Streamwise Grooves," AIAA Paper 2002-0978, Jan. 2002.

[6] Smith, A. N., Babinsky, H., Dhanasekaran, P. C., Savill, A. M., and Dawes, W. N., "Computational Investigation of Groove Controlled ShockWave/Boundary Layer Interaction," AIAA Paper 2003-0446, Jan. 2003.

[7] Jaiman, R., Loth, E., and Dutton, J., "Simulations of Normal Shock-Wave/Boundary-Layer Interaction Control Using Mesoflaps," *Journal of Propulsion and Power*, Vol. 20, No. 2, March–April 2004, pp. 344–352. doi:10.2514/1.9258

[8] Gefroh, D., Loth, E., Dutton, C., and McIlwain, S., "Control of an Oblique Shock/Boundary-Layer Interaction with Aeroelastic Mesoflaps," *AIAA Journal*, Vol. 40, No. 12, Dec. 2002, pp. 2456–2466.
doi:10.2514/2.1589

[9] Babinsky, H., Li, Y., and Pitt-Ford, C. W., "Microramp Control of Supersonic Oblique Shock Wave/Boundary Layer Interactions," *AIAA Journal*, Vol. 47, No. 3, March 2009, pp. 668–675.
doi:10.2514/1.38022

[10] McCormick, D. C., "Shock/Boundary-Layer Interaction Control with Vortex Generators and Passive Cavity," *AIAA Journal*, Vol. 31, No. 1, Jan. 1993, pp. 91–96.
doi:10.2514/3.11323

[11] Lin, J. C., "Review of Research on Low-Profile Vortex Generators to Control Boundary-Layer Separation," *Progress in Aerospace Sciences*, Vol. 38, Nos. 4–5, May–July 2002, pp. 389–420.
doi:10.1016/S0376-0421(02)00010-6

[12] Ashill, P. R., Fulker, J. L., and Hackett, K. C., "A Review of Recent Developments in Flow Control," *The Aeronautical Journal*, Vol. 109, No. 1095, 2005, pp. 205–232.

[13] Lee, S., Loth, E., and Wang, C., "LES of Supersonic Turbulent Boundary Layers with μVGs", AIAA Paper 2007-3916, June 2007.

[14] Shinn, A. F., Vanka, S. P., Mani, M., Dorgan, A., and Michal, T., "Application of BCFD Unstructured Grid Solver to Simulation of Micro-ramp Control of Shock/Boundary Layer Interactions," AIAA Paper 2007-3914, June 2007.

[15] Choi, J.-I., Oberoi, R. C., Edwards, J. R., and Rosati, J. A., "An Immersed Boundary Method for Complex Incompressible Flows," *Journal of Computational Physics*, Vol. 224, 2007, pp. 757–784.
doi:10.1016/j.jcp.2006.10.032

[16] Menter, F. R., "Zonal Two Equation k-ω Turbulence Models for Aerodynamic Flows," AIAA Paper 93-2906, July 1993.

[17] Menter, F. R., "Two-Equation Eddy-Viscosity Turbulence Models for Engineering Applications," *AIAA Journal*, Vol. 32, No. 8, Aug. 1994, pp. 1598–1605.
doi:10.2514/3.12149

[18] Edwards, J. R., and Liou, M.-S., "Low Diffusion Flux Splitting Methods for Flow at all Speeds," *AIAA Journal*, Vol. 36, No. 9, 1998, pp. 1610–1617.
doi:10.2514/2.587

[19] Colella, P., and Woodward, P. R., "The Piecewise Parabolic Method (PPM) for Gas-Dynamical Simulations," *Journal of Computational Physics*, Vol. 54, No. 1, 1984, pp. 174–201.
doi:10.1016/0021-9991(84)90143-8

[20] Wilcox, D. C., *Turbulence Modeling for CFD*, 2nd ed., DCW Industries, La Cañada, CA, 1998.

J. Sahu
Associate Editor